

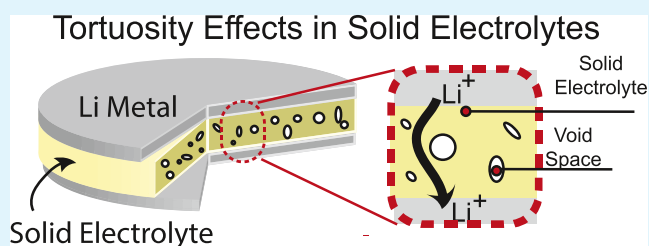
Tortuosity Effects in Garnet-Type $\text{Li}_7\text{La}_3\text{Zr}_2\text{O}_{12}$ Solid Electrolytes

Marm B. Dixit,[†] Matthew Regala,[†] Fengyu Shen,^{†,§} Xianghui Xiao,^{||} and Kelsey B. Hatzell^{*,†,‡,§,||}[†]Department of Mechanical Engineering, [‡]Chemical and Biomolecular Engineering, and [§]Interdisciplinary Material Science Program, Vanderbilt University, Nashville, Tennessee 37240, United States^{||}National Synchrotron Light Source II, Brookhaven National Laboratory, Upton, New York 11973, United States

S Supporting Information

ABSTRACT: Intrinsic material microstructure features, such as pores or void spaces, grains, and defects can affect local lithium-ion concentration profiles and transport properties in solid ion conductors. The formation of lithium-deficient or -excess regions can accelerate degradation phenomena, such as dendrite formation, lithium plating, and electrode/electrolyte delamination. This paper evaluates the effects pores or void spaces have on the tortuosity of a garnet-type $\text{Li}_7\text{La}_3\text{Zr}_2\text{O}_{12}$ solid electrolyte. Synchrotron X-ray tomography is used to obtain three-dimensional reconstructions of different electrolytes sintered at temperatures between 1050 and 1150 °C. The magnitude of the electrolyte tortuosity and the tortuosity directional anisotropy is shown to increase with sintering temperature. Electrolytes with highly anisometric tortuosity have lower critical current densities. Alignment or elimination of pores within an electrolyte or composite cathode may provide a means for achieving higher critical current densities and higher power densities in all solid-state batteries.

KEYWORDS: solid electrolyte, tortuosity, tomography, transport, microstructure



1. INTRODUCTION

Lithium metal is the ideal choice for the anode in a lithium-ion battery because it has the highest theoretical capacity (3860 mAh/g) and lowest electrochemical potential (−3.04V vs standard hydrogen electrode).^{1,2} All solid-state batteries may provide an avenue for enabling lithium-metal batteries if a solid separator (electrolyte) could be engineered to be thin (20–200 μm),³ strong (≥ 8 GPa),⁴ and highly ion conducting (10^{-3} S/cm).^{5–7} The rapid development of structural families of highly conducting solid electrolytes, including agryodites,^{8–10} garnets,¹¹ and LISICON/NASICON-type structures,^{12–14} has stimulated research in solid-state batteries. However, competitive energy densities and long lifetimes are necessary to displace the current state-of-the-art (liquid-based) batteries.

Poor power densities in all solid-state batteries are associated with low ionic conductivity in the solid electrolyte. However, recent advances from the material science and inorganic chemistry communities have led to new solid electrolytes that are competitive with liquid electrolytes. Thus, the low energy densities and power densities are likely due to ineffective transport at the numerous interfaces in a solid-state battery. There are two types of interfaces that exist in a solid-state battery: (1) intrinsic and (2) extrinsic. Intrinsic interfaces are natural interfaces that occur in a material (i.e., between grains, between grains and defects, and between grains and void spaces), and extrinsic interfaces occur at material junctions (electrode/electrolyte).^{15,16} The nature of transport at these interfaces can contribute to kinetic or mass transport limitations within the assembly¹⁷ and can lead to large

localized concentration and polarization gradients and accelerated failure. Examples of extrinsic interface instabilities include: (1) chemical decomposition and the formation of a solid electrolyte interphase at the electrode/electrolyte interface,^{18,19} (2) regions of excess and deficient lithium content,^{20,21} and (3) poor or delaminating-type contact at the interface that can contribute to nonuniform current distributions and localized degradation.^{22–25} Each of these phenomena are likely to cause catastrophic cell failure (short circuit) through the formation of dendrites. Understanding how these interfaces and defects contribute to transport limitations in all solid-state batteries will enable design strategies for high-performance batteries.

Lithium-ion transport occurs through the electrolyte-filled pore phase in conventional battery systems with polymer separators (Figure 1b).^{26–28} In contrast, the pore phase in a solid-state battery is ion blocking because ions only transport through the solid, bulk electrolyte phase (Figure 1a).^{1,29} The presence of void phases acts as roadblocks to ion migration and decreases the flux through the system. Furthermore, these void spaces lead to the formation of highly tortuous pathways in the electrolyte and nonuniform ion distribution in the system. These generate strong, local concentration and polarization gradients in the system and can lead to electrolyte degradation. Density functional theory (DFT) studies have shown that the

Received: September 25, 2018

Accepted: December 14, 2018

Published: December 18, 2018

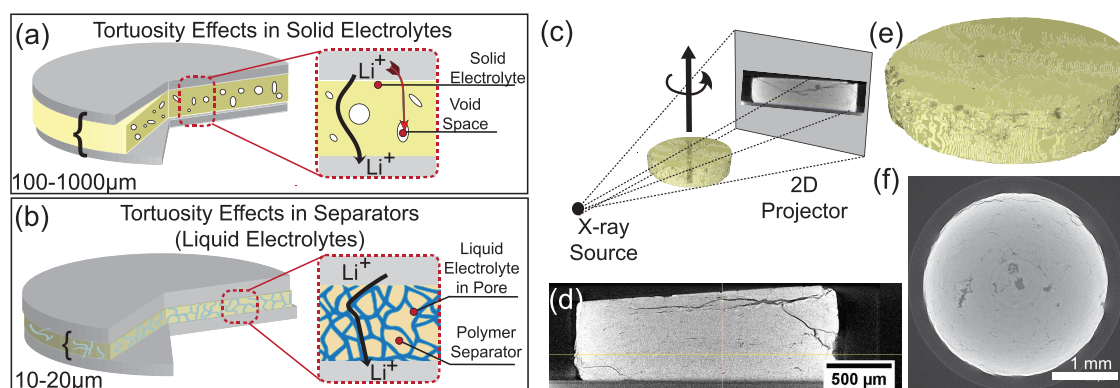


Figure 1. Tortuosity in a solid electrolyte is largely impacted by the formation of void phases or defects that emerge during processing (a). A porous separator in a traditional battery; the pore region is filled with liquid electrolyte (b). Synchrotron X-ray tomography enables probing the underlying microstructure of dense solid electrolyte characterized by heavy elements (c). A side view (d), a representative three-dimensional (3D) reconstruction (e), and a cross-sectional view of a solid electrolyte imaged at the Advanced Photon Source (f).

presence of such regions inside the electrolytes can lead to lithium-metal deposition, especially near cracks and pores.³⁰ Contradicting reports on the impact of grain microstructure on ion transport are seen in the literature.^{31–33} Further advancement of solid-state batteries requires an acute understanding about how ions move within a solid state electrolyte (SSE) and strategies for controlling transport. The solid electrolyte tortuosity is a critical parameter that governs the effective transport properties. Tortuosity in battery electrodes is widely studied and follows the empirical Bruggeman relationship.³⁴ Directional and anisometric tortuosity can emerge in battery electrodes as a result of the active material morphology. Directional tortuosity can affect the attainable power density in a battery and local transport rates. The latter mechanism can contribute to accelerated failure in battery systems.^{35,36}

Tortuosity is conventionally estimated either with electrochemical methods^{37,38} or by computational modeling of microstructures obtained with advanced imaging methods (X-ray tomography or focused ion beam scanning electron microscopy (FIB-SEM)).^{39,40} Effective transport properties derived using electrochemical techniques can be scaled to describe tortuosity in an electrode or electrolyte. These methods are comparatively quick and inexpensive.^{41–44} However, these methods are less versatile at obtaining local or directional information. Tortuosity estimation from microstructural data can provide unique insight into local transport anisotropy and can help pinpoint bottlenecks to transport. There are several studies that focus on measuring tortuosity in composite cathodes for all solid-state batteries. The cathode for a solid-state battery is unique in that it contains the active material in addition to a glass and/or ceramic ion conductor. Results using analytical techniques reveal that lower tortuosity and better power densities are achieved when the ion-conducting phase represents $\geq 40\%$ of the cathode phase.⁴³ Studies using FIB-SEM^{29,45} emphasize the impact of the cathode microstructure on cell performance. The presence of void phases that emerge because there is no liquid electrolyte in the electrode contributes to increases in the tortuosity. Overcoming these challenges (void phase formation) at extrinsic interfaces (electrode/electrolyte) will require advanced processing and manufacturing techniques.

Although there is a growing interest in understanding the impact of extrinsic interfaces on transport in all solid-state batteries, there are numerous intrinsic interfaces in solid

electrolytes that play a significant role on ion transport. These intrinsic interfaces include boundaries between grains, between grains and defects, and between grains and void spaces within the solid electrolyte and can govern localized concentration and polarization gradients within the cell. Understanding and controlling concentration gradients across the solid electrolytes as well as at the solid/solid interface is paramount for long lasting solid-state batteries. Tortuosity is studied in electrodes because it can limit the material utilization (energy density) and power performance in battery systems. Understanding tortuosity in a solid electrolyte is important because it can describe degradation mechanisms. Directional and anisometric tortuosity in a solid electrolyte may contribute to the formation of concentration “hot spots” at the electrode interface and drive degradation mechanisms. In this study, we investigate the tortuosity of garnet-type $\text{Li}_7\text{La}_3\text{Zr}_2\text{O}_{12}$ electrolytes with “real” and “ideal” pore configurations with the specific aim of understanding the impact of microstructure on the tortuosity of the solid electrolyte. The microstructure of different garnet-type electrolytes processed between 1050 and 1150 °C are obtained using synchrotron X-ray tomography (Figure 1c).^{1,46} The use of high-energy X-rays enables full penetration of the sample and the generation of 3D microstructures with submicron resolutions (Figure 1d–f). COMSOL and an open-source software TauFactor enable simulations of ionic fluxes in the solid electrolyte.⁴⁰ We evaluate idealized electrolyte microstructures (generated in silico) to probe the impact of pore ordering (symmetry and packing) on ionic transport properties.

2. EXPERIMENTAL SECTION

2.1. Material Synthesis and Electrochemical Studies.

$\text{Li}_7\text{La}_3\text{Zr}_2\text{O}_{12}$ (LLZO) was prepared with a mechanochemical synthesis method described previously.¹ Briefly, stoichiometric quantities of lithium, lanthanum, and zirconium salts were ball-milled with 10% excess lithium to mitigate lithium evaporation during the heating step. The ball-milled powder was sintered at 900 °C for 6 h. This powder was subsequently ball-milled again to reduce the particle sizes. Pellets (10 mm) were made from this powder using a pellet press. The green pellets were sintered at four different temperatures: 1000, 1050, 1100, and 1150 °C for 6 h. All sintering was carried out in alumina crucibles. The initial green density for the pellets was $51 \pm 1\%$. Cubic LLZO is obtained for all sintering temperatures, as evidenced by X-ray diffraction (XRD) (Figure S1). The sintered pellets were polished using a sand paper to a thickness of $\sim 500 \mu\text{m}$. The pellets were polished down to 3–4 mm diameter to facilitate the

tomography studies and ensure adequate transmission. Ionic conductivities were measured using an ion blocking symmetric setup. Impedance measurements were carried out between 1 MHz and 1 Hz with 50 mV amplitude. Li-metal disks were scratched and melted on to LLZO pellets on a hot plate. Li/LLZO/Li symmetric cells were assembled into a coin cell for galvanostatic charge–discharge tests. Charge–discharge cycles of 1 h duration were run with periodically increasing current until failure was observed.

2.2. X-ray Tomography. Synchrotron X-ray tomography was carried out at 2-BM beamline of Advanced Photon Source at Argonne National Laboratory. Detailed experimental methods have been previously reported.¹ Tomography projections were obtained during 180 °C of sample rotation with filtered white beam from synchrotron radiation. Reconstructions, ring, and zinger removal were carried out using TomoPy software.⁴⁷ Binarization and subsequent data analysis has been carried out in ImageJ.⁴⁸ Cubical subdomains of side 50 μm were extracted from the entire reconstruction. At least three subdomains of each sample were evaluated to obtain statistics for the estimated physical properties. BoneJ plugin⁴⁹ was employed to estimate the porosity and pore-size distributions of the solid electrolytes. The resolution for all experiments is 0.65 μm.

2.3. Ideal Domains. In addition to the development of real domains derived from X-ray tomography, ideal domains were developed in 3D computer-assisted design modeling software to enable understanding the effect of packing and arrangement on ion transport in these systems. Isotropic domains (50 μm³) of body-centered cubic (BCC), face-centered cubic (FCC), and hexagonal close-packed (HCP) structures were generated. Anisotropic domains including a parallelepiped (PP) structure consisting of tubular pores along the XX direction were also constructed. Domains of these structures were developed at porosities ranging from 0.625 to 60%. Analysis of parallelepiped structures was also conducted with a constant porosity of 50% but varying the number and orientation of tubes in a pattern. Additionally, domains of body-centered cubic structures with different numbers of unit cells were compared to determine if the number of unit cells played a part in isotropic systems.

2.4. Computational Fluid Modeling. Computational fluid modeling was performed using COMSOL Multiphysics. Segmented binary pore structures obtained from tomography were fed to COMSOL. Solid LLZO phase for computation was obtained by subtracting the segmented domains obtained from tomography from regular cubic domains within COMSOL. Alternatively, for ideal cases, the domain geometry was directly imported into COMSOL. Subsequently, the geometry was subjected to refinement and cleaning to produce the meshed domains. Domain volumes of 50 μm³ were created. A typical mesh was contained between 10⁵–5 × 10⁵ elements and 2 × 10⁴–3 × 10⁴ vertices. Due to the complex nature of the imaged pore networks, the refinement and cleaning steps necessary for each mesh were different. Three domains were evaluated for samples sintered at each temperature, and the average values are reported. Small concentrations were applied along the three principal axes for each domain. The following equation was solved during the simulations

$$\frac{\partial c}{\partial t} + \nabla N_i = R_i \quad (1)$$

$$N_i = -D_i \nabla c_i \quad (2)$$

where c_i is the concentration of species i , t is time, N_i is total flux, R_i is reaction source term, and D_i is the diffusion coefficient of species i . The steady-state flux and the effective diffusion coefficient were computed using eq 2. This effective diffusion coefficient was correlated to the primary diffusion coefficient with the formula⁵⁰

$$D_m = \frac{D_i}{\tau^2} \quad (3)$$

where D_m is the effective diffusion coefficient, D_0 is the ideal diffusion coefficient, and τ is the tortuosity. D_0 was computed from the

Nernst–Einstein equation for LLZO and was found to be 2.15⁻¹¹ m²/s.

3. RESULTS AND DISCUSSION

The underlying microstructure of LLZO influences ion transport and electrochemical properties in the electrolyte.¹ Porosity and pore sizes of the electrolytes have been obtained from the reconstructed tomography data. Porosity decreases with increasing sintering temperature due to denser packing of the material (Table 1). However, the largest observed pore size

Table 1. Physical and Electrochemical Properties of LLZO Electrolytes

sintering temperature (°C)	porosity (%)	pore size (μm)	grain size (μm)	conductivity (μS/cm)	C.C.D. ¹ (μA/cm ²)
1000	24		1	0.54	>90
1050	14	8	2	3.9	40
1100	8	9	30	81.1	12
1150	7	12	150	97.9	15

is seen to increase with increasing sintering temperature. This can be correlated to the electrochemical performance of the material system. The total ionic conductivity of LLZO increases from 0.54 μS/cm for the sample sintered at 1000 °C to 97.9 μS/cm for the sample sintered at 1150 °C (Figure S2). The increase in conductivity arises from the denser material packing seen in the system.^{51,52} In contrast, the critical current density is found to decrease from ~90 to ~15 μA/cm² for these samples.¹ Understanding differences in transport through these varying microstructures can provide a lens into understanding the impact of micropores on local ionic and polarization gradients.

The pore network for the sample sintered at 1050 °C shows a smaller discrete pore network (Figure 2a). The pore network for the sample sintered at 1000 °C could not be obtained from the tomography data. This could be due to the pore size in this sample falling under the resolution of the beamline (0.65 μm). As the sintering temperature is increased, the pore sizes are increased and a greater connectivity is observed in the pore structure (Figure 2b,c). These color maps represent the size of the pores in the microstructure. This is further confirmed by evaluating the local thickness of the solid phase in the three samples. Local thickness is defined as the radius of the largest sphere that can be inscribed at a point while remaining within the domain.⁵³ Cross-sectional views of local thickness are shown, with lighter regions signifying larger local thickness (solid-phase region) (Figure 2d–f). The local thickness maps depict the distance between the pores in the domain. The sample sintered at 1050 °C shows largest light regions, suggesting a larger solid domain. The intensity and spread of local thickness decreases with increasing sintering temperature, suggesting that the solid phase in the samples sintered at 1150 °C is less contiguous and is interspersed by the pore network. The pore networks shown here are representative volumes to highlight the differences in the microstructure. The average porosity trend is consistent with the experimentally measured porosities (Archimedes' method), as previously reported,¹ and decreases with increasing sintering temperature. Microstructural growth in solid electrolytes is strongly linked to the processing conditions. Hot-pressing the powders to generate pellets can lower the pore sizes while increasing the

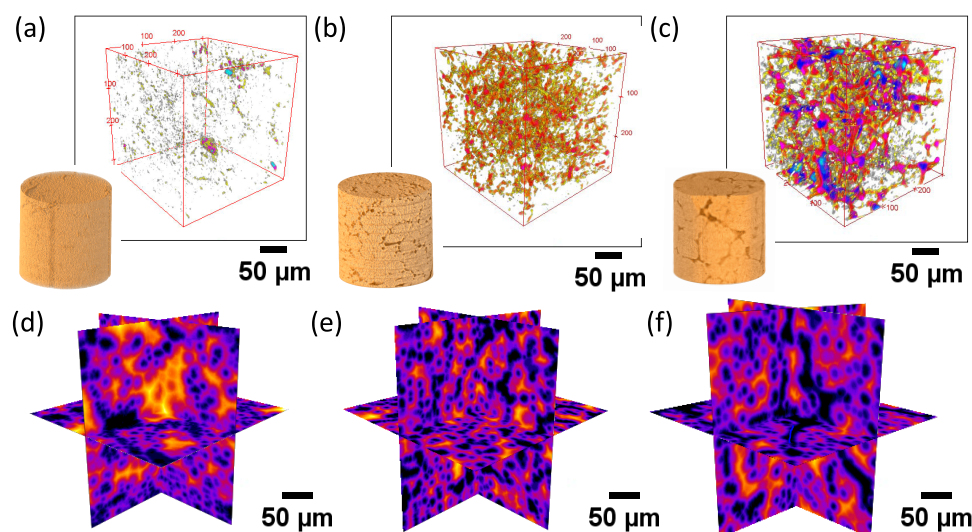


Figure 2. Pore-size color maps for solid state electrolyte (SSE) microstructures computed from reconstructed tomography sintered at (a) 1050, (b) 1100, and (c) 1150 °C. These represent the size of the pores in the microstructure. Distance maps for microstructure computed from reconstructed tomography data for SSEs sintered at (d) 1050, (e) 1100, and (f) 1150 °C. Lighter regions represent larger regions with connected solid phase. Dark regions represent short distances between pores. These represent the thickness of the solid phase connecting the pores. Three-dimensional rendering of the electrolytes are also shown.

density.^{31,33} Application of pressure during sintering can lead to removal of pores with better grain growth.

Mass transport in electrolytic systems can be described with the movement of mobile ionic species, material balances, current flow, and electroneutrality. The flux density in a typical electrolyte can be given as⁵⁴

$$N_i = -z_i u_i F c_i \nabla \Phi - D_i \nabla c_i \quad (4)$$

where N_i is the flux of species i , z_i is the valency of species i , u_i is the mobility of species i , F is Faraday's constant, c_i is the concentration of species i , $\nabla \Phi$ is the potential gradient, ∇c_i is the concentration gradient for species i , and D_i is the diffusion constant. The first term on the right-hand side of eq 4 represents the migration term, whereas the second term represents the diffusion term. Typically, these driving forces act in opposing directions and the transport of ions depend on the net electrochemical potentials. The effective transport properties need to be scaled by tortuosity to capture microstructure-driven effects.⁵⁵ To estimate the tortuosity through the solid electrolytes, it is necessary to compute the flux of Li ion through the samples. Only concentration gradients are applied in the simulation studies to reduce the computational efforts required. Incorporating both the driving forces in the simulation greatly increases the complexity due to the interdependence of the variables and exponentially increases the computing power required. Since tortuosity is a property of the microstructure, neglecting the electric driving force in the system should not influence its measurement. Thus, the reduced form of eq 4, i.e., eq 1, and the material balance in eq 2 are solved.

The results shown are for sample domains of $50 \times 50 \times 50 \mu\text{m}^3$ size. Increasing the sample domain size to $100 \times 100 \times 100 \mu\text{m}^3$ does not significantly change the simulated tortuosity values for samples sintered at 1050 and 1100 °C, whereas the tortuosity values for the sample sintered at 1150 °C show a slight increase (Figure S4 and Table S1). The dependence of physical properties on the domain subvolume has been previously reported.^{1,56} However, meshing of the reconstructed

domains is extremely difficult for these larger volumes and subsequent computing power necessitated did not allow for studying domains larger than $100 \times 100 \times 100 \mu\text{m}^3$. Lithium-ion flux is found to be uniformly distributed along the three principal axes for the sample sintered at 1050 °C. This arises from the fact that this sample has small pore sizes ($8 \mu\text{m}$) that are dispersed through the material. The simulated tortuosity in this case is close to one and identical for all directions (Figure 3a and Table 2). At 1100 °C, anisotropy in Li-ion flux is observed, with the sample showing higher flux along the YY

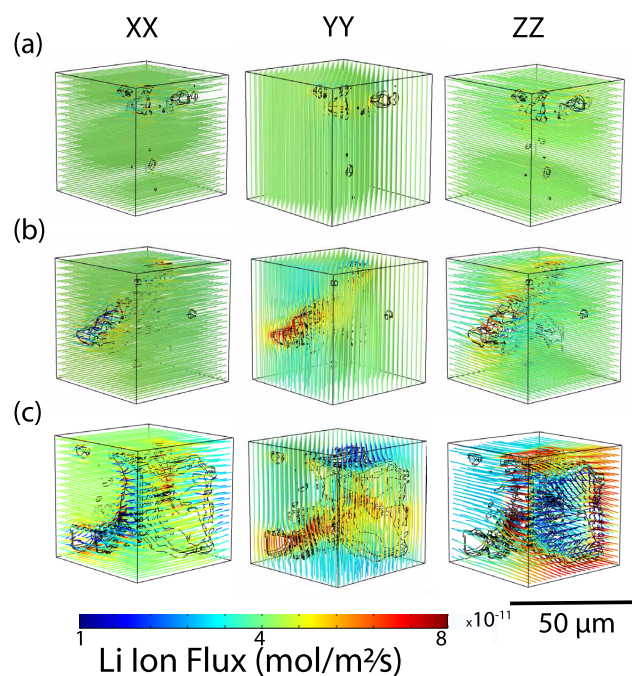


Figure 3. Li-ion flux streamlines along three principal axes for microstructural domains of real LLZO electrolytes sintered at (a) 1050, (b) 1100, and (c) 1150 °C.

Table 2. Simulated Tortuosity for LLZO Electrolytes

sintering temperature (°C)	XX	YY	ZZ
1050	1.00	1.00	1.00
1100	1.02 ± 0.01	1.03 ± 0.01	1.03 ± 0.00
1150	1.05 ± 0.07	1.07 ± 0.09	1.06 ± 0.08

directions in certain regions compared to *XX* and *ZZ* directions. Correspondingly, small variations are seen in the tortuosity of the system along the three directions. At 1150 °C, the pore cluster size is large and considerable variations in Li-ion flux are observed along the three principle axes. The large, clustered pores lead to a nonuniform distribution of Li-ion flux, and higher values and wider spread are observed in the tortuosity along the three directions compared with the samples sintered at lower temperatures.

The anisotropic flux distribution arising due to higher tortuosity leads to a significant variation in the local concentration of Li ions in the electrolyte for the samples sintered at 1150 °C. This results in strong concentration and polarization gradients at the edges of the pore structures. DFT studies suggest that the presence of excess electrons on pore surfaces can enable lithium-metal reduction.³⁰ These localized electrons on pore surfaces coupled with the strong concentration gradients arising from nonuniform mass transport can initiate deposition of lithium into the pores. These results confirm earlier work and shed light on the lower critical current densities observed in these samples ($\approx 15 \mu\text{A}/\text{cm}^2$).¹ The samples sintered at lower temperatures do not show this anisotropic flux distribution and hence show higher critical current densities ($\approx 40 \mu\text{A}/\text{cm}^2$). The sample sintered at 1150 °C shows initiation of degradation at $12 \mu\text{A}/\text{cm}^2$ with eventual failure at $15 \mu\text{A}/\text{cm}^2$, whereas the sample sintered at 1100 °C fails at $12 \mu\text{A}/\text{cm}^2$ (Figure S3). The slight increase of C.C.D. from 1100 to 1150 °C suggests presence of competing mechanisms that drive failure. Apart from the microstructure-driven failure mechanism discussed here, interfacial contact, local defects, grain structure, and orientation can lead to generation of lithium-deficient and enriched zones that can affect the failure mechanism. These factors could potentially be the reason for the lower C.C.D. values observed for samples sintered at 1100 °C compared to those for samples sintered at 1150 °C.

Tortuosity factors evaluated using the open-source package TauFactor were used to corroborate simulated values. The tortuosity factor computed with TauFactor is determined from the ratio of steady-state diffusive flux through a pore network F_p to that of an equivalent fully dense control volume with the same physical properties. The software computes these fluxes using the following equations

$$F_p = -A_{CV}D \frac{\epsilon \Delta C}{\tau L_{CV}} \quad (5)$$

$$F_{CV} = -A_{CV}D \frac{\Delta C}{L_{CV}} \quad (6)$$

where D is the diffusivity of the dense phase, C is the local concentration, and A_{CV} and L_{CV} are cross-sectional area and the length of the control volume, respectively. The software considers each voxel as a distinct mesh element, which mitigates the need for resampling and meshing. The samples sintered at 1050 °C show a uniform distribution of flux through the three principal directions (Figure 4a). The images

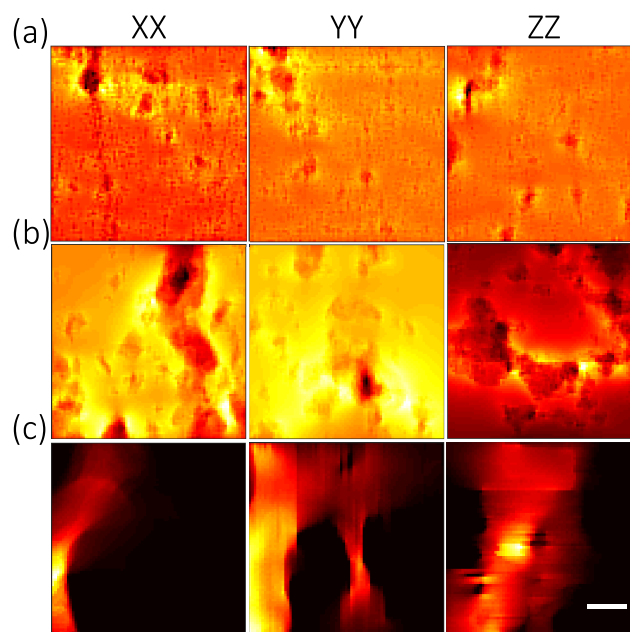


Figure 4. Projection of the total flux along three principal axes for real LLZO electrolytes sintered at (a) 1050 °C, (b) 1100 °C, and (c) 1150 °C. The scale bar is 50 μm and is common for all figures. The same domains shown in Figure 3 are used for this analysis. These results are obtained from TauFactor software.

represent the sum of the flux through the three principal directions projected onto a single slice. Brighter regions represent regions with high flux. The tortuosity value predicted by the software was ~ 1.01 in all directions. For the samples sintered at 1100 °C, the simulated tortuosity values increased to ~ 1.06 and directional anisotropy becomes apparent along the *ZZ* direction where very low flux (high tortuosity) is observed (Figure 4b). This corroborates well with the simulated data (Figure 3b). Large directional anisotropy and significantly higher tortuosity values were observed for the samples sintered at 1150 °C. Tortuosity values predicted by this software were 9.13, 2.03, and 2.76 along the *XX*, *YY*, and *ZZ* directions. Although these values are considerably higher than those observed by the earlier method, the trends are consistent. Both methods confirm that the magnitude of the electrolyte tortuosity and the anisotropy in directional tortuosity increase with increasing sintering temperature. The differences in tortuosity values predicted from the two methods could arise due to meshing differences as well as computational differences in the two methods.

Ideal solid electrolytes are completely dense with 0% porosity. However, practically achieving perfectly dense electrolytes is challenging and requires energy-consuming high-temperature sintering processes. The previous sections highlighted how the concentration profiles and ionic flux are impacted by the presence of pores. Thus, there may be opportunities for tailoring the ionic pathway between the electrode and electrolyte via tailoring the pore size and distribution. Symmetry and alignment in pore structures have been leveraged to develop high-rate electrodes.⁵⁷ Three times higher specific capacities are attained in electrodes with aligned pores than nonarchitected electrodes. A similar principle can be leveraged in the design of solid electrolytes to enhance their rate performances.

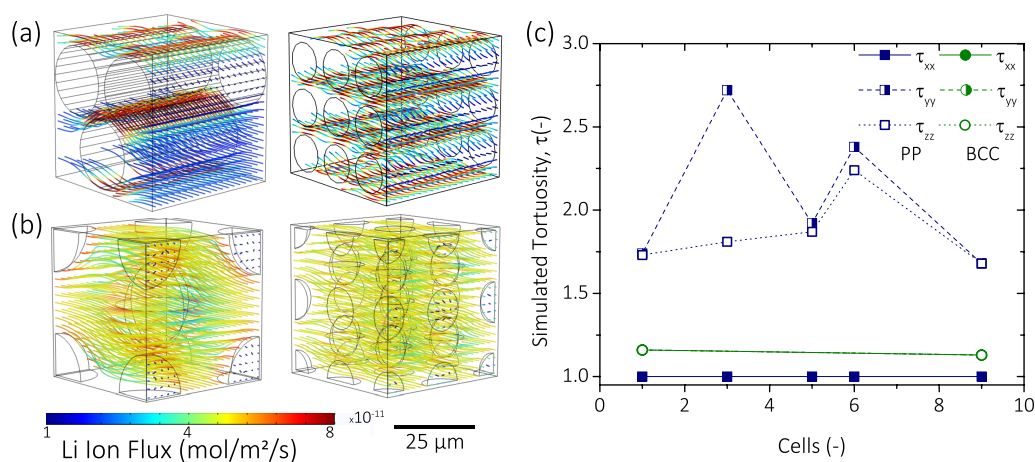


Figure 5. Investigation of model electrolyte structure for transport properties. Flux streamlines for parallelepiped pore configurations with three and nine pore units at constant porosity (a). Flux streamlines for BCC pore configurations with one and nine pore units at constant porosity (b). Simulated tortuosities along three principal axes for parallelepiped and BCC pore configuration with varying pore units (c).

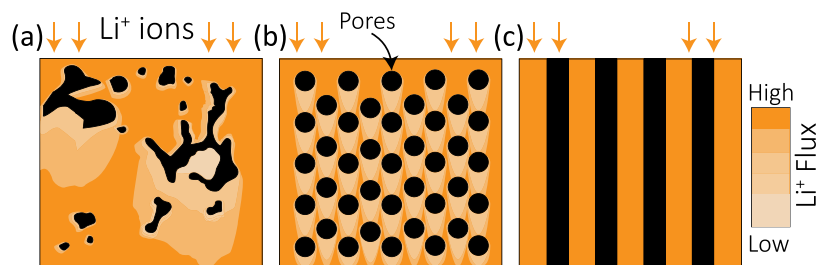


Figure 6. Distribution of lithium-ion flux through solid electrolyte for microstructures with (a) realistic pore network, (b) isotropic pore network, and (c) anisotropic pore network.

Pore microstructure in real samples is highly anisotropic, which leads to high tortuosity, as discussed previously. To investigate the impact of tailoring pore structure, domains with BCC, FCC, HCP, and PP configurations of pores developed in silico are investigated as ideal microstructures for solid electrolytes. Ideal microstructures are studied to extrapolate quantitative information regarding the impact of microstructure on ion transport and guide rational microstructure design of solid electrolytes. PP structure yields uniform striped fields along the direction of ion transport. This configuration is similar to the configuration identified as the upper bound for the Wiener constraints of effective transport properties of porous media.⁵⁸ The configuration can be equated to a parallel resistor network, leading to maximized transport in this configuration. The simulated tortuosity along the XX direction is ≈ 1 for the PP case due to this reason. Along the transverse (YY and ZZ) directions, the tortuosity is higher due to the obstructions arising due to the longitudinal pores. This can be equated to the lower-bound configuration of the Wiener constraints with phases arranged in a transverse fashion. This equates to a series resistance circuit lowering the effective transport. Increasing the number of pores at a constant porosity results in oscillating tortuosity along the transverse directions. This variation arises from generation of symmetric microstructures (equivalent to upper-bound configuration) within the domain. This can be visualized by the three-cell and nine-cell architectures for PP configuration (Figure 5a). Ion-flow paths have a symmetric arrangement along the YY direction (streamlines shown), leading to a low tortuosity value. However, nonsymmetric phase arrangement is observed

along the ZZ direction and the ion flow needs to be divided around each pore element, leading to an increased tortuosity in this direction. In contrast, the ion-flow path shows identical structures while transversing along YY and ZZ directions for nine-cell architecture and hence identical, low tortuosity values are seen.

The tortuosity values remain constant irrespective of the number of repeat units of the pore structure at a constant porosity (Figure 5b,c) for domains with isotropic distribution of pore structures. This results from uniform flow profiles that are generated around the pores. It is observed that BCC pore structure offers a higher average flux through the system with smaller gradients in the transverse direction. Much higher concentration gradients are seen along ion transport through transverse directions of PP pores, which can have a detrimental effect on the stability and electrochemical performance of the electrolyte, as discussed earlier. However, transport through parallelepiped domains along the direction of the pores results in maximum flux as well as uniform distribution (Figure S5). Real electrolyte microstructures are highly anisotropic with no regular shapes (Figure 6a). These result in strong flux gradients within the system that can lead to lithium deposition and failure. Isolated, isotropic pore domains (Figure 6b) alleviate some of these; however, flux gradients cannot completely be eliminated. Connected and aligned pore domains (Figure 6c) can theoretically achieve high and uniform flux distribution through the solid electrolytes. These results reinforce the importance of controlling the alignment and symmetry of pore domains in improving transport rates through the electrolyte.

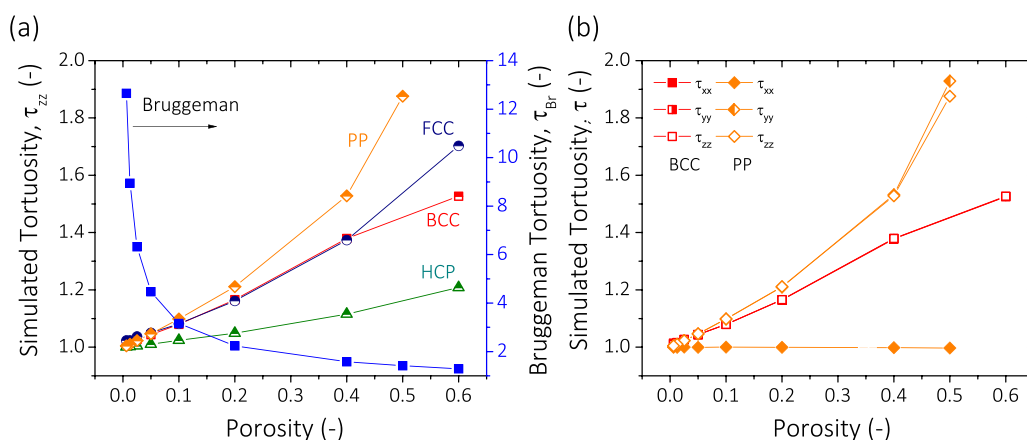


Figure 7. (a) Variation in simulated tortuosities along the ZZ direction for different pore configurations over a range of porosities. The Bruggeman tortuosity is also plotted on the secondary Y axis as a reference. (b) Directional anisotropy in tortuosity for the PP and BCC pore networks.

Tortuosity decreases with increased packing of the pores (FCC > BCC > HCP) for isotropic domains (Figures 7a and S6). This effect can be explained by the Hashin–Shtrikman constraints on effective transport properties of a porous medium.⁵⁸ According to these constraints, maximized transport can be achieved by core–shell type of configuration, with phase with lower conductivity occupying the core site. BCC, FCC, and HCP configurations achieve this kind of configuration and hence show lower tortuosity and higher transport rates. Further, HCP configuration results in the highest packing for the solid phase and subsequently shows the lowest tortuosity values. Experimental studies show increasing critical current densities with decreasing LLZO particle size.⁵⁹ Reducing the particle size improves the packing of the solid phase in a way similar to the HCP configuration. To further understand the effect of packing configurations, domains with a wide range of porosities were simulated to enable predictions of porosity–tortuosity relationships for solid electrolytes. The tortuosity increases with increasing porosity, as expected. Modifying the Bruggeman relationship⁶⁰ to reflect that the transport occurs through the solid phase, we get

$$\tau = (1 - \epsilon)^{(1-\alpha)} \quad (7)$$

Using this equation, the exponent α is estimated to be 1.457, 1.59, and 1.209 for BCC, FCC, and HCP pore structures (Figures 7b and S6). A reasonable fit is obtained for all datasets using these values. Further, these values are consistent over the three directions for these three microstructures. This is expected as these possess isotropic pore distributions. Bruggeman exponents can be correlated to the connectivity of the transport phase, with higher Bruggeman exponent values signifying lower connectivity.⁶¹ HCP configuration shows the lowest Bruggeman exponent, implying a well-connected solid phase. This result corroborates the higher flux rates observed in this configuration. FCC configuration shows the highest Bruggeman exponent, indicating a less connected domain. In contrast, the Bruggeman exponent is 1, 1.93, and 1.89 in XX, YY, and ZZ directions for the PP case. The exponent of 1 along the XX direction signifies a fully connected solid phase, which is optimum for transport. Further, the wide spread of Bruggeman exponents shows the impact of alignment and symmetry in reducing the tortuosity. On the basis of these results, it is proposed that architecturing pores along the direction of ion transport can help reduce the tortuosity and

maximize the flux through the system. Further work on engineering this kind of microstructures with solid electrolytes is needed.

4. CONCLUSIONS

The effect of microstructure on ion transport in LLZO solid electrolytes was evaluated. Computational fluid dynamic simulations are run on COMSOL Multiphysics software to evaluate the tortuosity factor. Samples sintered at lower temperatures have discrete pore structure with small feature sizes that lead to homogenous flux distributions within the sample. Samples sintered at higher temperatures show larger pore sizes with a connected pore network. These samples show higher tortuosity as well as greater directional anisotropies. These lead to development of large local concentration and polarization gradients that can initiate and accelerate failures in these systems. The tortuosity factor values are further corroborated with an open-source software. Ideal pore microstructures are evaluated by in silico development of computational domains with BCC, FCC, HCP, and PP distributions. Aligned pores along the transport direction can minimize tortuosity and improve the rate performance of solid-state electrolytes.

■ ASSOCIATED CONTENT

Supporting Information

The Supporting Information is available free of charge on the ACS Publications website at DOI: 10.1021/acsami.8b16536.

XRD patterns, electrochemistry data, additional simulation results (PDF)

■ AUTHOR INFORMATION

Corresponding Author

*E-mail: kelsey.b.hatzell@vanderbilt.edu. Phone: +1 (615)-875-8391.

ORCID

Kelsey B. Hatzell: 0000-0002-5222-7288

Notes

The authors declare no competing financial interest.

■ ACKNOWLEDGMENTS

The authors were supported by the National Science Foundation under grant No. 1727863. The authors acknowl-

edge the Vanderbilt Institute of Nanoscience and Engineering (VINSE) for access to their shared characterization facilities. This research used resources of the Advanced Photon Source, a U.S. Department of Energy (DOE) Office of Science User Facility operated for the DOE Office of Science by Argonne National Laboratory under Contract No. DE-AC02-06CH11357. This research used resources of the National Synchrotron Light Source, a U.S. Department of Energy (DOE) Office of Science User Facility operated for the DOE Office of Science by Brookhaven National Laboratory under Contract No. DE-AC02-98CH10886.

REFERENCES

- (1) Shen, F.; Dixit, M.; Xiao, X.; Hatzell, K. The Effect of Pore Connectivity on Li Dendrite Propagation Within LLZO Electrolytes Observed with Synchrotron X-ray Tomography. *ACS Energy Lett.* **2018**, *3*, 1056–1061.
- (2) Lin, D.; Liu, Y.; Cui, Y. Reviving the Lithium Metal Anode for High-Energy Batteries. *Nat. Nanotechnol.* **2017**, *12*, 194–206.
- (3) McCloskey, B. D. Attainable Gravimetric and Volumetric Energy Density of Li–S and Li Ion Battery Cells with Solid Separator-Protected Li Metal Anodes. *J. Phys. Chem. Lett.* **2015**, *6*, 4581–4588.
- (4) Monroe, C.; Newman, J. Dendrite Growth in Lithium/Polymer Systems. A Propagation Model for Liquid Electrolytes under Galvanostatic Conditions. *J. Electrochem. Soc.* **2003**, *150*, A1377–A1384.
- (5) Janek, J.; Zeier, W. G. A Solid Future for Battery Development. *Nat. Energy* **2016**, *1*, No. 16141.
- (6) Yu, C.; Ganapathy, S.; Van Eck, E. R.; Wang, H.; Basak, S.; Li, Z.; Wagemaker, M. Accessing the Bottleneck in All-Solid State Batteries, Lithium-Ion Transport Over the Solid-Electrolyte-Electrode Interface. *Nat. Commun.* **2017**, *8*, No. 1086.
- (7) Dawson, J. A.; Canepa, P.; Famprikis, T.; Masquelier, C.; Islam, M. S. Atomic-Scale Influence of Grain Boundaries on Li-Ion Conduction in Solid Electrolytes for All-Solid-State Batteries. *J. Am. Chem. Soc.* **2018**, *140*, 362–368.
- (8) Culver, S. P.; Koerver, R.; Krauskopf, T.; Zeier, W. G. Designing Ionic Conductors: The Interplay Between Structural Phenomena and Interfaces in Thiophosphate-Based Solid-State Batteries. *Chem. Mater.* **2018**, *30*, 4179–4192.
- (9) Wenzel, S.; Metelmann, H.; Raif, C.; Dürr, A. K.; Janek, J.; Adelhelm, P. Thermodynamics and Cell Chemistry of Room Temperature Sodium/Sulfur Cells with Liquid and Liquid/Solid Electrolyte. *J. Power Sources* **2013**, *243*, 758–765.
- (10) Wenzel, S.; Leichtweiss, T.; Krüger, D.; Sann, J.; Janek, J. Interphase Formation on Lithium Solid Electrolytes - An in situ Approach to Study Interfacial Reactions by Photoelectron Spectroscopy. *Solid State Ionics* **2015**, *278*, 98–105.
- (11) Murugan, R.; Thangadurai, V.; Weppner, W. Fast lithium Ion Conduction in Garnet-Type $\text{Li}_7\text{La}_3\text{Zr}_2\text{O}_{12}$. *Angew. Chem., Int. Ed.* **2007**, *46*, 7778–7781.
- (12) Kanno, R.; Murayama, M. Lithium Ionic Conductor Thio-LISICON: The $\text{Li}_2\text{S}-\text{GeS}_2-\text{P}_2\text{S}_5$ System. *J. Electrochem. Soc.* **2001**, *148*, A742–A746.
- (13) Kanno, R.; Hata, T.; Kawamoto, Y.; Irie, M. Synthesis of a New Lithium Ionic Conductor, Thio-LISICON-Lithium Germanium Sulfide System. *Solid State Ionics* **2000**, *130*, 97–104.
- (14) Bruce, P. G.; West, A. R. The A-C Conductivity of Polycrystalline LISICON, $\text{Li}_{2+2x}\text{Zn}_{1-x}\text{GeO}_4$, and a Model for Intergranular Constriction Resistances. *J. Electrochem. Soc.* **1983**, *130*, 662–669.
- (15) Hatzell, K. B.; Dixit, M. B.; Berlinger, S. A.; Weber, A. Z. Understanding Inks for Porous-Electrode Formation. *J. Mater. Chem. A* **2017**, *5*, 20527–20533.
- (16) Dixit, M.; Harkey, B.; Shen, F.; Hatzell, K. B. Catalyst Layer Ink Interactions that Affect Coatibility. *J. Electrochem. Soc.* **2018**, *165*, F264–F271.
- (17) Kasemchainan, J.; Peter, G. All-Solid-State Batteries and their Remaining Challenges. *Johnson Matthey Technol. Rev.* **2018**, *62*, 177–180.
- (18) Lotsch, B. V.; Maier, J. Relevance of Solid Electrolytes for Lithium-Based Batteries: A Realistic View. *J. Electroceram.* **2017**, *38*, 128–141.
- (19) Han, F.; Zhu, Y.; He, X.; Mo, Y.; Wang, C. Electrochemical Stability of $\text{Li}_{10}\text{GeP}_2\text{S}_{12}$ and $\text{Li}_7\text{La}_3\text{Zr}_2\text{O}_{12}$ Solid Electrolytes. *Adv. Energy Mater.* **2016**, *6*, No. 1501590.
- (20) Wang, J.; Guo, Z.; Xiong, S. Characterization of the Morphology of Primary Silicon Particles using Synchrotron X-Ray Tomography. *Mater. Charact.* **2017**, *123*, 354–359.
- (21) Wang, Z.; Santhanagopalan, D.; Zhang, W.; Wang, F.; Xin, H. L.; He, K.; Li, J.; Dudney, N.; Meng, Y. S. In situ STEM-EELS Observation of Nanoscale Interfacial Phenomena in All-Solid-State Batteries. *Nano Lett.* **2016**, *16*, 3760–3767.
- (22) Ohta, N.; Takada, K.; Sakaguchi, I.; Zhang, L.; Ma, R.; Fukuda, K.; Osada, M.; Sasaki, T. LiNbO_3 -Coated LiCoO_2 as Cathode Material for All Solid-State Lithium Secondary Batteries. *Electrochem. Commun.* **2007**, *9*, 1486–1490.
- (23) Takada, K.; Nakano, S.; Inada, T.; Kajiyama, A.; Sasaki, H.; Kondo, S.; Watanabe, M. Compatibility of Lithium Ion Conductive Sulfide Glass with Carbon-Lithium Electrode. *J. Electrochem. Soc.* **2003**, *150*, A274–A277.
- (24) Zheng, J.; Dang, H.; Feng, X.; Chien, P.-H.; Hu, Y.-Y. Li-ion Transport in a Representative Ceramic–Polymer–Plasticizer Composite Electrolyte: $\text{Li}_7\text{La}_3\text{Zr}_2\text{O}_{12}$ –Polyethylene Oxide–Tetraethylene Glycol Dimethyl Ether. *J. Mater. Chem. A* **2017**, *5*, 18457–18463.
- (25) Zheng, J.; Hu, Y.-Y. New Insights into the Compositional Dependence of Li-Ion Transport in Polymer–Ceramic Composite Electrolytes. *ACS Appl. Mater. Interfaces* **2018**, *10*, 4113–4120.
- (26) Lagadec, M. F.; Ebner, M.; Zahn, R.; Wood, V. Technique for Visualization and Quantification of Lithium-Ion Battery Separator Microstructure. *J. Electrochem. Soc.* **2016**, *163*, A992–A994.
- (27) Lagadec, M. F.; Zahn, R.; Wood, V. Designing Polyolefin Separators to Minimize the Impact of Local Compressive Stresses on Lithium Ion Battery Performance. *J. Electrochem. Soc.* **2018**, *165*, A1829–A1836.
- (28) Zahn, R.; Lagadec, M. F.; Hess, M.; Wood, V. Improving Ionic Conductivity and Lithium-Ion Transference Number in Lithium-Ion Battery Separators. *ACS Appl. Mater. Interfaces* **2016**, *8*, 32637–32642.
- (29) Hlushkou, D.; Reising, A. E.; Kaiser, N.; Spannenberger, S.; Schlabach, S.; Kato, Y.; Roling, B.; Tallarek, U. The Influence of Void Space on Ion Transport in a Composite Cathode for All-Solid-State Batteries. *J. Power Sources* **2018**, *396*, 363–370.
- (30) Tian, H. K.; Xu, B.; Qi, Y. Computational Study of Lithium Nucleation Tendency in $\text{Li}_7\text{La}_3\text{Zr}_2\text{O}_{12}$ (LLZO) and Rational Design of Interlayer Materials to Prevent Lithium Dendrites. *J. Power Sources* **2018**, *392*, 79–86.
- (31) Sharafi, A.; Haslam, C. G.; Kerns, R. D.; Wolfenstine, J.; Sakamoto, J. Controlling and Correlating the Effect of Grain Size with the Mechanical and Electrochemical Properties of $\text{Li}_7\text{La}_3\text{Zr}_2\text{O}_{12}$ Solid-State Electrolyte. *J. Mater. Chem. A* **2017**, *5*, 21491–21504.
- (32) Cheng, L.; Chen, W.; Kunz, M.; Persson, K.; Tamura, N.; Chen, G.; Doeff, M. Effect of Surface Microstructure on Electrochemical Performance of Garnet Solid Electrolytes. *ACS Appl. Mater. Interfaces* **2015**, *7*, 2073–2081.
- (33) David, I. N.; Thompson, T.; Wolfenstine, J.; Allen, J. L.; Sakamoto, J. Microstructure and Li–Ion Conductivity of Hot-Pressed Cubic $\text{Li}_7\text{La}_3\text{Zr}_2\text{O}_{12}$. *J. Am. Ceram. Soc.* **2015**, *98*, 1209–1214.
- (34) Chung, D.-W.; Ebner, M.; Ely, D. R.; Wood, V.; García, R. E. Validity of the Bruggeman Relation for Porous Electrodes. *Modell. Simul. Mater. Sci. Eng.* **2013**, *21*, No. 074009.
- (35) Ebner, M.; Chung, D.-W.; García, R. E.; Wood, V. Tortuosity Anisotropy in Lithium Ion Battery Electrodes. *Adv. Energy Mater.* **2014**, *4*, No. 1301278.

- (36) Kehrwald, D.; Shearing, P. R.; Brandon, N. P.; Sinha, P. K.; Harris, S. J. Local Tortuosity Inhomogeneities in a Lithium Battery Composite Electrode. *J. Electrochem. Soc.* **2011**, *158*, A1393–A1399.
- (37) Thorat, I. V.; Stephenson, D. E.; Zacharias, N. A.; Zaghbi, K.; Harb, J. N.; Wheeler, D. R. Quantifying Tortuosity in Porous Li-Ion Battery Materials. *J. Power Sources* **2009**, *188*, 592–600.
- (38) Vijayaraghavan, B.; Ely, D. R.; Chiang, Y.-M.; García-García, R.; García, R. E. An Analytical Method to Determine Tortuosity in Rechargeable Battery Electrodes. *J. Electrochem. Soc.* **2012**, *159*, A548–A522.
- (39) Ebner, M.; Wood, V. Tool for Tortuosity Estimation in Lithium Ion Battery Porous Electrodes. *J. Electrochem. Soc.* **2015**, *162*, A3064–A3070.
- (40) Cooper, S. J.; Bertei, A.; Shearing, P. R.; Kilner, J. A.; Brandon, N. P. TauFactor: An Open-Source Application for Calculating Tortuosity Factors from Tomographic Data. *SoftwareX* **2016**, *5*, 203–210.
- (41) Landesfeind, J.; Ebner, M.; Eldiven, A.; Wood, V.; Gasteiger, H. A. Tortuosity of Battery Electrodes: Validation of Impedance-Derived Values and Critical Comparison with 3D Tomography. *J. Electrochem. Soc.* **2018**, *165*, A469–A476.
- (42) Landesfeind, J.; Eldiven, A.; Gasteiger, H. A. Influence of the Binder on Lithium Ion Battery Electrode Tortuosity and Performance. *J. Electrochem. Soc.* **2018**, *165*, A1122–A1128.
- (43) Kaiser, N.; Spannenberger, S.; Schmitt, M.; Cronau, M.; Kato, Y.; Roling, B. Ion Transport Limitations in All-Solid-State Lithium Battery Electrodes Containing a Sulfide-Based Electrolyte. *J. Power Sources* **2018**, *396*, 175–181.
- (44) Kato, Y.; Shiotani, S.; Morita, K.; Suzuki, K.; Hirayama, M.; Kanno, R. All-Solid-State Batteries with Thick Electrode Configurations. *J. Phys. Chem. Lett.* **2018**, *9*, 607–613.
- (45) Choi, S.; Jeon, M.; Ahn, J.; Jung, W. D.; Choi, S. M.; Kim, J.-S.; Lim, J.; Jang, Y.-J.; Jung, H.-G.; Lee, J.-H.; Sang, B.-I.; Kim, H. Quantitative Analysis of Microstructures and Reaction Interfaces on Composite Cathodes in All-Solid-State Batteries Using a Three-Dimensional Reconstruction Technique. *ACS Appl. Mater. Interfaces* **2018**, *10*, 23740–23747.
- (46) Hatzell, K. B.; Eller, J.; Morelly, S. L.; Tang, M. H.; Alvarez, N. J.; Gogotsi, Y. Direct Observation of Active Material Interactions in Flowable Electrodes using X-Ray Tomography. *Faraday Discuss.* **2017**, *199*, 511–524.
- (47) Gürsoy, D.; De Carlo, F.; Xiao, X.; Jacobsen, C. TomoPy: A Framework for the Analysis of Synchrotron Tomographic Data. *J. Synchrotron Radiat.* **2014**, *21*, 1188–1193.
- (48) Schneider, C. A.; Rasband, W. S.; Eliceiri, K. W. NIH Image to ImageJ: 25 Years of Image Analysis. *Nat. Methods* **2012**, *9*, 671–675.
- (49) Münch, B.; Holzer, L. Contradicting Geometrical Concepts in Pore Size Analysis Attained with Electron Microscopy and Mercury Intrusion. *J. Am. Ceram. Soc.* **2008**, *91*, 4059–4067.
- (50) Shen, L.; Chen, Z. Critical Review of the Impact of Tortuosity on Diffusion. *Chem. Eng. Sci.* **2007**, *62*, 3748–3755.
- (51) Yamada, H.; Ito, T.; Basappa, R. H. Sintering Mechanisms of High-Performance Garnet-type Solid Electrolyte Densified by Spark Plasma Sintering. *Electrochim. Acta* **2016**, *222*, 648–656.
- (52) El-Shinawi, H.; Paterson, G. W.; MacLaren, D. A.; Cussen, E. J.; Corr, S. A. Low-Temperature Densification of Al-Doped $\text{Li}_7\text{La}_3\text{Zr}_2\text{O}_{12}$: A Reliable and Controllable Synthesis of Fast-Ion Conducting Garnets. *J. Mater. Chem. A* **2017**, *5*, 319–329.
- (53) Hildebrand, T.; Rügsegger, P. A New Method for the Model-Independent Assessment of Thickness in Three-Dimensional Images. *J. Microsc.* **1997**, *185*, 67–75.
- (54) Newman, J.; Thomas-Alyea, K. E. *Electrochemical Systems*; Wiley, 2012.
- (55) Doyle, M.; Newman, J.; et al. Comparison of Modeling Predictions with Experimental Data from Plastic Lithium Ion Cells. *J. Electrochem. Soc.* **1996**, *143*, 1890–1903.
- (56) Pietsch, P.; Ebner, M.; Marone, F.; Stampanoni, M.; Wood, V. Determining the Uncertainty in Microstructural Parameters Extracted from Tomographic Data. *Sustainable Energy Fuels* **2018**, *2*, 598–605.
- (57) Billaud, J.; Bouville, F.; Magrini, T.; Villeveille, C.; Studart, A. R. Magnetically Aligned Graphite Electrodes for High-Rate Performance Li-Ion Batteries. *Nat. Energy* **2016**, *1*, No. 16097.
- (58) Ferguson, T. R.; Bazant, M. Z. Nonequilibrium Thermodynamics of Porous Electrodes. *J. Electrochem. Soc.* **2012**, *159*, A1967–A1985.
- (59) Cheng, L.; Wu, C. H.; Jarry, A.; Chen, W.; Ye, Y.; Zhu, J.; Kostecky, R.; Persson, K.; Guo, J.; Salmeron, M.; Chen, G.; Doe, M. Interrelationships among Grain Size, Surface Composition, Air Stability, and Interfacial Resistance of Al-Substituted $\text{Li}_7\text{La}_3\text{Zr}_2\text{O}_{12}$ Solid Electrolytes. *ACS Appl. Mater. Interfaces* **2015**, *7*, 17649–17655.
- (60) Bruggeman, D. A. G. Berechnung Verschiedener Physikalischer Konstanten von Heterogenen Substanzen. I. Dielektrizitätskonstanten und Leitfähigkeiten der Mischkörper aus Isotropen Substanzen. *Ann. Phys.* **1935**, *416*, 636–664.
- (61) Vadakkepatt, A.; Trembacki, B.; Mathur, S. R.; Murthy, J. Y. Bruggeman's Exponents for Effective Thermal Conductivity of Lithium-Ion Battery Electrodes. *J. Electrochem. Soc.* **2016**, *163*, A119–A130.